Anwar *et al. Energy Mater.* **2025**, *5*, 500102
DOI: 10.20517/energymater.2025.16

Energy Materials

Article

Open Access

Check for updates

Electrochemical insights into performance enhancement of protonic ceramic fuel cells with $Ba(Zr,Ce,Y)O_{3-\delta}$ electrolyte

Muhammad Faisal Anwar[1,#], Yong Yu[2,#], Muhammad Khalid[1], Atif Nazar[1], Bushra Bibi[1], Muhammad Farrukh Sarfraz[1], Bin Zhu[1,2,*], Jianbing Huang[2,*], Muhammad Imran Asghar[3,*]

[1]School of Energy and Environment, Southeast University, Nanjing 210096, Jiangsu, China.
[2]State Key Laboratory of Multiphase Flow in Power Engineering, School of Energy and Power Engineering, Xi'an Jiaotong University, Xi'an 710049, Shaanxi, China.
[3]Renewable Energy Technologies Group, Faculty of Engineering and Natural Sciences, Tampere University, Tampere FI-33014, Finland.
[#]Authors contributed equally.

***Correspondence to:** Prof. Bin Zhu, School of Energy and Environment, Southeast University, Nanjing 210096, Jiangsu, China; State Key Laboratory of Multiphase Flow in Power Engineering, School of Energy and Power Engineering, Xi'an Jiaotong University, Xi'an 710049, Shaanxi, China. E-mail: zhu-bin@seu.edu.cn; Prof. Jianbing Huang, State Key Laboratory of Multiphase Flow in Power Engineering, School of Energy and Power Engineering, Xi'an Jiaotong University, Xi'an 710049, Shaanxi, China. E-mail: huangjb@mail.xjtu.edu.cn; Prof. Muhammad Imran Asghar, Renewable Energy Technologies Group, Faculty of Engineering and Natural Sciences, Tampere University, Tampere FI-33014, Finland. E-mail: imran.asghar@tuni.fi

How to cite this article: Anwar, M. F.; Yu, Y.; Khalid, M.; Nazar, A.; Bibi, B.; Sarfraz, M. F.; Zhu, B.; Huang, J.; Asghar, M. I. Electrochemical insights into performance enhancement of protonic ceramic fuel cells with $Ba(Zr,Ce,Y)O_{3-\delta}$ electrolyte. *Energy Mater.* **2025**, *5*, 500102. https://dx.doi.org/10.20517/energymater.2025.16

Received: 21 Jan 2025 **First Decision:** 14 Mar 2025 **Revised:** 19 Mar 2025 **Accepted:** 26 Mar 2025 **Published:** 16 May 2025

Academic Editors: Yizhong Huang, Yuping Wu **Copy Editor:** Fangling Lan **Production Editor:** Fangling Lan

Abstract

The burgeoning field of protonic ceramic fuel cells (PCFCs) is characterized by significant scientific and technological advancements, particularly with the incorporation of $BaZr_{0.1}Ce_{0.7}Y_{0.2}O_{3-\delta}$ (BZCY) as a proton-conducting electrolyte. In the modern energy materials field, the challenge is not only developing new materials but also understanding new mechanisms and gaining an in-depth understanding of their interaction with energy devices. To drive significant advances, it is crucial to address both material-specific challenges and device-level innovations that unlock the full potential of these materials. In this work, we introduced an electrochemical proton injection approach to successfully improve BZCY proton conductivity by an order of magnitude. We also delve into the electrode and interface kinetic processes and their interplay in proton transport within the bulk and grain boundary of the BZCY-electrolyte of PCFCs. These approaches have led to state-of-the-art advances, achieving a proton conductivity of 0.19 S cm^{-1} and a device peak power density of 943 mW cm^{-2} at 530 °C. Our results

demonstrate that the bulk and grain boundary conduction significantly mitigate polarization losses by four to five orders of magnitude, thereby accelerating the kinetic process and further contributing to improved PCFC performance. The appearance of peaks and alterations in relaxation times further illustrate the electrode reactions and proton transport mechanisms. Beyond providing a comprehensive assessment of current technological progress, this article underscores the transformative potential of electrochemical processes in PCFCs, positioning them as a cornerstone in the quest for sustainable and clean energy technologies.

Keywords: Protonic ceramic fuel cell, electrochemical proton injection, ionic conduction, electrolyte, hydrogen oxidation reaction, oxygen reduction reaction

INTRODUCTION

Electrochemical reactions play a crucial role in various applications including (photo)electrocatalysis, batteries, fuel cells, corrosion, electroplating, metal production, pseudocapacitors, and more. Fuel cells, particularly protonic ceramic fuel cells (PCFCs), stand as a testament to the remarkable progress in the domain of clean energy conversion technologies due to their high efficiency and environmental benefits, especially when operating at low temperatures (300-500 °C)[1-3]. Characterized by their high efficiency and fuel flexibility, PCFCs have captured the attention of the scientific community, driven by the imperative for sustainable energy solutions. Central to their operation is the electrolyte material, which plays a crucial role in dictating the overall performance and feasibility of the cell at various operating conditions. In the current landscape of energy materials for applications, the challenges lie not only in discovering new materials, but also developing new approaches and mechanisms, as well as in depth understanding of the interplay between materials and energy devices. To drive significant advances, it is crucial to address both material-specific challenges and device-level innovations that unlock the full potential of these materials.

To develop low-temperature PCFCs, significant efforts have been directed toward improving the proton conductivity of oxide ceramic electrolytes. Perovskite oxides have also been studied as electrolytes. The initial breakthrough came 40 years ago with the discovery of Iwahara *et al.* of $SrCeO_3$-based proton conductors, which showed a proton conductivity of 3×10^{-3} S cm^{-1} at 700 °C[4]. Extensive efforts have been made to enhance proton conductivity through structural doping. Remarkably, $BaCe_{0.9}Y_{0.1}O_{3-\delta}$ (BCY) possesses a significant proton conductivity of 2×10^{-2} S cm^{-1} at 600 °C[5].

In recent years, numerous efforts have been made to develop new families of oxide proton conductors as PCFC electrolytes. For example, a hexagonal perovskite-related oxide $Ba_5Er_2Al_2ZrO_{13}$ exhibits a proton conductivity of 10^{-3} S cm^{-1} across a wide temperature range from 300-1,200 °C[6]. Another notable example is the LISICON $Li_{13.9}Sr_{0.1}Zn(GeO_4)_4$, which shows a proton conductivity of 0.034 S cm^{-1} at 600 °C. Additionally, the proton conductivity can be further increased to 0.048 S cm^{-1} through Li^+/H^+ exchange process at the same temperature[7]. Grain boundaries/interfaces play a major role in increasing the ionic conductivity of YSZ/$SrTiO_3$ heterostructure[8]. This finding underscores the vital role of interfaces in advancing the performance of electrochemical systems by optimizing ionic pathways, potentially leading to more efficient energy conversion technologies. There is extensive research and developments on the surface/interface proton conduction in fluorite oxides that have proven successful in semiconductor ionic membrane fuel cells (SIMFCs)[9,10]. In this new type of PCFC, proton transport pathways are facilitated via surfaces/interfaces of oxide particles, enabling *in-situ* or low-temperature annealing of the electrolyte. Despite the presence of nano/micropores in the electrolyte, gas leakage can be minimized by using a thicker electrolyte with a three-dimensional tortuous pore structure, which also enhances the kinetics of the hydrogen oxidation reaction (HOR) and the oxygen reduction reaction (ORR)[11]. These ongoing advancements in perovskite oxide proton conductors have significantly propelled the development of PCFCs and reversible

protonic ceramic electrochemical cells, moving them toward applications in energy conversion and storage[12,13]. However, further improvements of materials are essential not only to achieve the higher proton conductivities which requires a proton conductivity of 0.1 S cm^{-1} for the electrolyte, but also active electrode catalyst materials for efficient PCFC operation at low-temperatures, 300-500 °C[14].

To solve these challenging issues, recent advances on research and development have highlighted layered structured $Ni_{0.8}Co_{0.15}Al_{0.05}LiO_2$ (NCAL) as a promising electrode material due to its excellent electrocatalytic properties[15]. NCAL addresses the gap in electrocatalyst functions required for temperatures ranging from 300 to 500 °C without using traditional noble metal or perovskite-based electrode materials which are used in conventional low-temperature polymer electrolyte membrane fuel cells (PEMFCs) or high-temperature solid oxide fuel cells (SOFCs)/PCFCs. The NCAL electrode has shown excellent catalytic activity for both the ORR and HOR[16]. The three-dimensional porous structure of the NCAL electrode significantly increases the surface area available for electrochemical reactions[17]. The multi-transition element nature of NCAL induces a favorable distribution of electrocatalyst sites and facilitates a better electrode-electrolyte interface[18]. Additionally, the NCAL has exhibited a triple charge ($H^+/O^{2-}/e^-$) conducting properties to enhance electrocatalytic activity[19].

Recent developments have introduced a novel approach to create high proton conduction pathways along oxide ion-conducting Gd-doped CeO_2 (GDC) by leveraging a synergistic H^+ and O^{2-} transport mechanism at low temperatures. GDC is traditionally known as an O^{2-} conductor[20] with conductivity 0.1 S cm^{-1} at 800 °C, but now it has been optimized as a predominant H^+ conductor, achieving a protonic conductivity of 0.158 S cm^{-1} at 500 °C, outperforming many other oxide proton conductors[21]. These advancements in proton-conducting GDC electrolyte and highly catalytic NCAL electrodes can facilitate efficient low-temperature (300-500 °C) PCFC research and development.

Emerging as a promising alternative, proton-conducting perovskite materials such as $Ba(Zr,Ce,Y)O_{3-\delta}$ (BZCY) have led to the development of PCFCs. BZCY has been extensively reported in the literature often without fundamental innovations in understanding the material-device interactions and mechanisms. As a result, the full potential of PCFC technology remains underutilized. As a fact, $BaCe_{0.8-x}Zr_xY_{0.2}O_{3-\delta}$ (BZCY) presents significant oxygen vacancy due to Y^{3+} doped Zr^{4+}, which has some inherent O^{2-} mobility via oxygen vacancy mechanism, Such O^{2-} transport properties exhibit as intrinsic nature in oxygen (air) atmosphere and high temperatures (above 800 °C). In temperatures and the existence of the moisture or hydrogen atmosphere, protons take the majority of transport properties. From this aspect of consideration, some similarities to the above GDC displayed synergistic H^+ and O^{2-} transport. Performance enhancements in PCFCs are predominantly catalyzed by advancements in the electrochemical dynamics within the cell. The intricate processes of the HOR at the anode and the ORR at the cathode are paramount to the energy conversion efficiency of cells. The pursuit of improving these processes, especially at low-temperature operations, continues to be a critical area of research, as it holds the key to unlocking the full potential of PCFCs.

Despite these advances, optimizing reaction kinetics at low temperatures (300-500 °C) remains a critical challenge and also unprecedented research in PCFCs, where this study can certainly make significant contributions. Current work provides a comprehensive model that fully integrates the intricate interplay of electron and proton transfers specific to PCFC electrodes and proton transport through the membrane. Our current efforts are devoted to deepening insights into HOR, ORR, and proton transport using the newly developed proton-conducting BZCY electrolyte for PCFC. The complexity of the HOR and ORR, coupled with their sensitivity to the electrolyte's material characteristics, necessitates a nuanced approach to

electrochemical analysis. In particular, BZCY electrolytes have shown promise in facilitating these reactions by taking their surface or grain boundary proton conductivity.

We have taken a fresh look at the BZCY electrolyte, focusing on a more profound understanding of both the material and the PCFC device. Introducing an electrochemical proton injection (EPI) method significantly improves material proton conductivity. Additionally, we investigate the electrochemical performance and its relation to material properties to unlock the interdependencies between them, which is crucial for optimizing device performance. We employed a comprehensive research methodology that integrates electrochemical impedance spectroscopy (EIS) and distribution of relaxation times (DRT) analysis to elucidate HOR, ORR, and proton transport mechanisms in 300-500 °C PCFCs. EIS and DRT analysis allows us to dissect the charge transfer resistance (R_{ct}), resolve overlapping processes, and identify individual time constants, providing a detailed understanding of reaction kinetics and polarization losses. These combined techniques offer comprehensive electrochemical insights, enabling the optimization of electrocatalysts and reduction of polarization losses, ultimately enhancing the performance and efficiency of low-temperature PCFCs. This paper provides an in-depth electrochemical analysis of BZCY-based PCFCs, focusing on the dynamic processes that lead to performance enhancement. Through this analysis, we aim to offer insights that could drive the design of next-generation PCFCs.

EXPERIMENTAL SECTION

Fuel cell fabrication

Fuel cell electrodes were prepared by coating a thin layer of commercial NCAL (Tianjin Bamo Science & Technology Joint Stock Ltd., China) on nickel foam (Ni-NCAL). A mixture of 5 g NCAL electrode material and 0.1 g polyvinylidene fluoride (PVDF, binder for electrode particles) was ground in a mortar pestle followed by the addition of 1.5 mL terpineol to form NCAL electrode slurry. The slurry was used to prepare a layer of it on Ni foam and dried in the oven at 120 °C for 45 min. The resultant Ni-NCAL electrodes were used for both anode and cathode. The fuel cell devices were assembled via a dry press procedure. In this process, 0.25 g of $BaZr_{0.1}Ce_{0.7}Y_{0.2}O_{3-\delta}$ (BZCY) was used as an electrolyte material. Electrolyte with thickness of 400 μm (Supplementary Figure 1 shows scanning electron microscope (SEM) image) was sandwiched between two electrodes in a symmetrical configuration of Ni-NCAL/BZCY/NCAL-Ni under a pressure range of 378 MPa to get a final 1.5 mm thick symmetrical cell with an active area of 0.64 cm^2. Three cells, Cell-1, Cell-2, and Cell-3, were prepared with the same material and configuration.

Further, we used an alternative fabrication method (assembled method) to compare the proton conductivities under different atmospheres. In this approach, a fuel cell was fabricated using 1,500 °C sintered BZCY electrolyte and 500 °C annealed BZCY electrolyte. For the assembled method, BZCY pellets were prepared by pressing the 0.5 g powder at 350 MPa, and heat-treated at 1,500 °C and 500 °C for 2 h to get sintered and annealed BZCY electrolyte pellets, respectively, and the electrolyte thickness was 800 μm. Then, the complete cells were assembled by sandwiching a BZCY pellet with 2 Ni-NCAL electrodes in a fuel cell testing holder. Prior to EIS measurements, all cells having Ni-NCAL/BZCY/NCAL-Ni configuration were preheated to 550 °C for 1 h.

Electrochemical measurement

To investigate the transition from electronic-dominant conduction to proton-dominant conduction in the material, EIS analysis was performed. EIS experiments were conducted at various temperatures (410, 440, 470, 500, 520 and 550 °C). For Cell-1, hydrogen is employed as fuel and supplied to the anode side at a flow rate of 100 mL min^{-1}. Air is used as the oxidant on the cathode side with same flow rate of 100 mL min^{-1}. Polarization curves were measured with the help of an electronic load. The data was recorded using IT7500

software. The EIS analysis of cell-2 with a similar configuration Ni-NCAL/BZCY/NCAL-Ni was performed at a temperature of 500 °C. Cell-2 is preheated to 550 °C for approximately 1 h prior to EIS followed by cooling to 500 °C. EIS was performed with controlled gas flow rates at the electrodes. Subsequently, air is provided on both electrodes (anode and cathode) and EIS was conducted again for comparison. It provides insights into the ORR. Similarly, Cell-3 with configuration Ni-NCAL/BZCY/NCAL-Ni was heated for about 1 h, and mixture of Nitrogen (N_2) and Hydrogen (H_2) is applied on both sides of the cell with different concentrations (10%, 20%, 30%, 40%, and 50%) followed by EIS measurements at 500 °C.

Methodologies

To analyze the electrochemical process regarding HOR and ORR occurring in a fuel cell under different atmospheres (H_2/air, H_2 + N_2, and air/air), an equivalent circuit model was used to capture ORR for air/air and HOR for H_2 + N_2. This involves a circuit with multiple components and parameters, viz., R_{ct} for each reaction and double layer capacitance (C_{dl}). We analyzed the differences in R_{ct} values for HOR and ORR under various atmospheres to indicate changes in reaction kinetics. In the fuel cell environment, changes in R_{ct} and other parameters were interpreted based on the known electrochemical behavior of HOR and ORR, considering gas composition and electrode performance. The presence of oxygen in the air/air environment affects ORR kinetics, while the absence of oxygen in the H_2 + N_2 environment influenced reaction kinetics, with intricacies in R_{ct} and other parameters observed in the context of the HOR process. C_{dl} reflects the capacitance of the electrical double layer at the electrode interface and it can be influenced by the changes in the electrochemical process, particularly when considering the adsorption and desorption of species involved in the electrochemical reactions. Warburg Impedance (Z_w) is associated with the diffusion of species in the electrolyte and can be indicative of the transport of ions and charge carriers involved in the electrochemical process. Impedance data were fitted and calculated by Z-view software. Nyquist plots are used as a tool in identifying electrochemical processes relevant to HOR and ORR.

In the context of the DRT analysis, several corresponding investigations such as polarization resistance and timescales associated with electrochemical processes were carried out to gain insights into the electrochemical process. By identifying the relaxation times associated with different processes in the system, such as proton transfer, electron transfer, and other relevant charge carrier movements, it is possible to discern the characteristic timescales of various electrochemical steps. DRT analysis is used to simplify impedance spectra and to improve the accuracy of analysis. By establishing correlations between the extracted DRT parameters and the known charge transfer mechanisms, it becomes possible to relate the identified relaxation times to the timescales associated with proton and electron transfer steps. This can aid in understanding how changes in the DRT parameters reflect alterations in the rate-determining steps of the electrochemical process within the fuel cell system. The DRT method was computed by the MATLAB GUI tool to analyze EIS data. The Gaussian process was utilized to manage data noise, overlapped timescale features, discontinuous data, and inductive characteristics from a probabilistic perspective. This computation relies on Tikhonov regularization along with continuous function discretization. This method effectively addresses the limitations of conventional DRT through regularization techniques[22]. Regularization parameter was selected as 10^{-4} and excluded the inductance. A suitable shape factor of 0.5 was selected to mitigate the occurrence of pseudo peaks, ensuring smoother data interpretation and more efficient post-processing of DRT deconvoluted results[22-24]. Following model is used to fit the EIS data:

$$F(\tau) = \frac{-\ln(10)}{\pi}\left[Z''\left(e^{-\ln\tau+\frac{j\pi}{2}}\right) + Z''\left(e^{-\ln\tau-\frac{j\pi}{2}}\right)\right] \quad (1)$$

where Z'' is related to imaginary part of Z, τ is the relaxation time which refers to the frequency by $\tau = \frac{1}{2\pi f}$ and $F(\tau)$ is the distribution function following

$$\int_{-\infty}^{\infty} F(\tau) d log_{10}\tau = Z'(0) - Z'(\infty) \quad (2)$$

where $Z'(0)$ - $Z'(\infty)$ is equal to the whole polarization resistance. Contribution of various electrochemical processes become visible in $F(\tau)$ and $log_{10}\tau$ plot. The relaxation time and resistance data were obtained following the acquisition of the peak segmentation results. Comparing the actual results with calculated results, chemical processes related to each peak were determined because these processes overlapped in EIS has distinct data characteristics (resistance, capacitance, frequency and relaxation time).

Electrochemical proton injection

Electrochemical proton injection (EPI) was conducted through a fuel cell apparatus to investigate the dynamics of electrochemical reactions using a controlled, limited flow of H_2 in fuel cell activation process. The PCFC anodic reaction ($H_2 \leftrightarrow 2H^+ + 2e^-$) produces proton resources via an electrocatalyst electrode in an electrochemical manner for EPI. This methodology is essential because commonly used proton ceramic oxides, such as perovskites BZCY, lack intrinsic proton defects and cannot achieve proton conductivity in an air atmosphere. These ceramic oxides require a hydrogen or proton-containing environment such as moisture, humidity, hydrogen, or protons produced by the electrocatalyst reaction (HOR) in the EPI we proposed, to exhibit proton conductivity. Therefore, EPI is crucial for studying and developing advanced proton-conducting ceramic oxides and relevant PCFC processes. The controlled flow of H_2 enables the examination of proton transport dynamics via EIS and DRT analysis. DRT methodology investigates the conducting transition from intrinsic oxygen-ion conduction to the preferential proton injection over time. Once injected into the electrolyte, proton transport mechanisms were analyzed using DRT, which was applied to real-time EIS data collection during the fuel cell activation. DRT analysis decomposes the EIS spectrum into its constituent relaxation times, helping to segregate and pinpoint various electrochemical processes such as HOR, ORR, and proton transport mechanisms. Proton injection occurred at different time scales, coinciding with the stabilization of conductivities. Distinct peaks in DRT signify different electrochemical processes, with their areas calculated through integration to gauge the polarization resistance of individual processes. Alterations in peak intensity or position reflect the evolution of the fuel cell's electrochemical processes as the atmospheric conditions shift from air/air to H_2/air. This analysis aids in unraveling the details of electrochemical reactions and transport processes within the fuel cell, and understanding their reliance of these processes on operational conditions and time.

RESULTS AND DISCUSSION

Mechanistic insights

Figure 1 offers a schematic illustration of HOR at anode, ORR at cathode and proton conduction through bulk and grain boundaries. The left panel (a) displays the NCAL surface interacting with hydrogen molecules during the anode process (HOR). The hydrogen molecules (H_2) approach the NCAL surface, where they are adsorbed and dissociated into protons (H^+) and electrons (e^-). The protons are likely to migrate through the electrolyte, while the electrons are conducted away through the external circuit. The NCAL catalyst surface is represented with multicolored spheres indicating various elements of the catalyst material. Indicated by arrows, protons move through the electrolyte toward the cathode side.

The right panel illustrates the NCAL surface during the cathode process. Similar to the anode side, the catalyst surface is depicted with a combination of spheres representing the NCAL structure. Here, oxygen

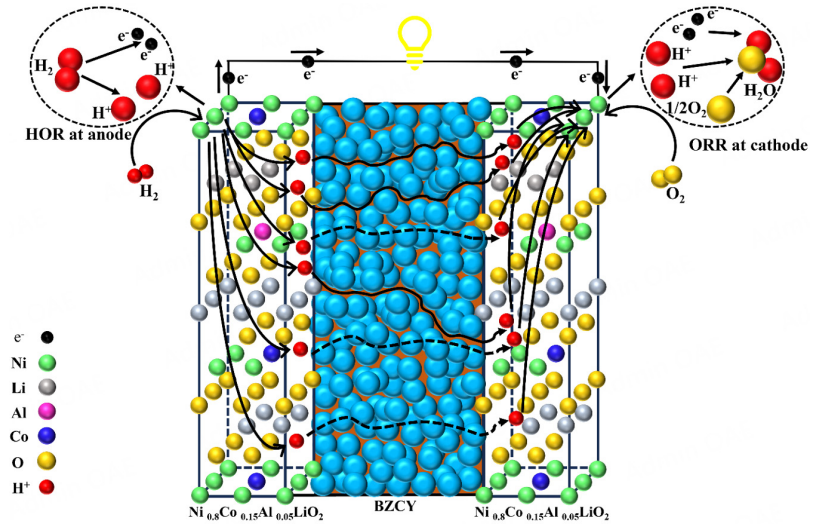

Figure 1. Schematic illustration of hydrogen oxidation reaction (HOR) at anode, oxygen reduction reaction (ORR) at cathode and proton conduction through bulk and grain boundaries.

molecules (O_2) from the air interact with the NCAL surface, undergoing a reduction process (ORR) where they combine with protons (coming from the electrolyte) and electrons (from the external circuit) to form water (H_2O). Solid lines in BZCY electrolyte show the large grain boundary conduction while thin and dashed lines demonstrate the bulk conduction. Arrows indicate protons and electrons moving toward the catalyst surface, where they participate in the ORR to produce water. The product of the reaction, water molecules, are shown diffusing away from the catalyst surface.

The overall process is presented in a step-wise manner to clearly show the path of reactants (hydrogen and oxygen) as they undergo electrochemical reactions at the surface of the catalyst and protons conduct through bulk and grain boundaries from the electrolyte. These processes are central to the operation of a fuel cell, with HOR occurring at the anode where fuel is oxidized, and ORR occurring at the cathode where oxygen is reduced, collectively driving the generation of electricity.

In general, H^+ can migrate through oxide materials via two primary mechanisms: the Grothuss or hopping mechanism and the vehicle mechanism. In the hopping mechanism, protons can travel between immobile oxygen ions. In contrast, vehicle mechanism involves the transport of protons through OH^- or H_3O^+ ions[25]. The vehicle mechanism involves the creation of OH^- ion and an oxygen vacancy ($V_o^{\bullet\bullet}$) within oxide structure. Conventionally, defect chemistry relies on equilibrium processes such as hydration or hydrogenation mechanisms as per following reactions, respectively:

$$H_2O + O_{lattice}^X + V_o^{\bullet\bullet} \leftrightarrow 2OH_{lattice}^{\bullet} \quad (3)$$

$$H_2(g) + 2O_o^X \leftrightarrow 2OH_{lattice}^{\bullet} + 2e' \quad (4)$$

Surface hydroxyl species ($OH_{lattice}^{\bullet}$) are produced as a result of hydration process. While in the hydrogenation process, H_2 gas plays a role in defect chemistry and generates $OH_{lattice}^{\bullet}$ with concurrent electron injection. Both of the processes include indirect proton injection. Apart from conventional studies, we used the EPI approach, which bypasses the H_2O/H_2 equilibrium processes and directly injects protons into the electrolyte. The protons ($H^{\bullet}$), which are generated at the anode via HOR ($H_2 \leftrightarrow 2H^{\bullet} + 2e'$), are injected into the oxide

lattice, where they can interact with lattice oxygen ($O^X_{lattice}$), forming proton defects such as hydroxyl groups ($OH^{\bullet}_{lattice}$). This process is crucial for the transport of protons within the material. This process of creating proton defects involves a redox reaction known as protonation. The direct proton injection in EPI modifies the defect chemistry as per following reaction:

$$H^{\bullet} + O^X_{lattice} \leftrightarrow OH^{\bullet}_{lattice} \quad (5)$$

Here, $H^{\bullet}$ is introduced directly as a dynamic species, with its transport pathways governed by grain boundaries and surfaces, unlike traditional bulk equilibrium conditions. EPI can investigate the dynamic behavior of H^+ in real time, enabling the study of transitions from intrinsic O^{2-} conduction to H^+-dominant conduction under H_2/air.

The overall reaction in the PCFC oxygen electrode is given as follows:

$$1/2O_2(g) + 2H^{\bullet} + 2e' \leftrightarrow H_2O \quad (6)$$

which was divided into a series of five elementary reaction steps[26] and then modified into multi-reaction processes[27]. This reaction sequence is commonly used to assign a polarization process consisting of one or more of the suggested reaction steps.

Fuel cell measurement

I-V and corresponding *I-P* curves for fuel cell devices with Ni-NCAL/BZCY/NCAL-Ni configuration are demonstrated in Figure 2. The cell with the BZCY electrolyte achieves peak power densities of 943, 805, 633, 478, 321 and 213 $mWcm^{-2}$ at 530, 500, 470, 440, 410 and 380 °C, respectively. These performance curves are a critical tool in evaluating the effectiveness of BZCY as an electrolyte for fuel cells, particularly in terms of its electrical conductivity and ability to facilitate the electrochemical reactions necessary for power generation. Figure 2 provides insight into the efficiency of the cell designs tested and allows for the comparison of the electrochemical performance of BZCY under various conditions.

Electrochemical impedance spectroscopy

Figure 3A shows the electrochemical impedance spectroscopy (EIS) spectrum of fuel cells at different temperatures under H_2/air atmosphere. Experimental results were fitted and analyzed by using multiple components; viz., R_b corresponds to bulk resistance, and R_{gb} denotes grain boundary resistance. Constant phase elements (CPEs) correspond to non-ideal capacitance. The bulk R_b resistance can be obtained at the starting point of the grain boundary arc from the impedance spectra measured. The detailed fitted results are listed in Supplementary Table 1. R_b, $R_{gb,}$ and R_{ct} were determined to be 0.1632, 0.0378, and 0.125 Ω cm^2 at 530 °C, respectively, with gradual increase to 0.2102, 0.2183 and 1.35 Ω cm^2 at 380 °C, respectively. R_b increased with decrease in the temperature because ionic transportation is a thermal activated process.

C_{dl} was calculated using CPEs, as given by

$$C_i = \frac{[R_i \times CPE - T_i]^{1/CPE-P_i}}{R_i} \quad (7)$$

where *C* is the relevant capacitance, *R* is the corresponding resistance, and *CPE - T* and *CPE - P* are CPEs representing quasi-capacitance and arc slope indicating deviation from the ideal capacitive behavior, respectively.

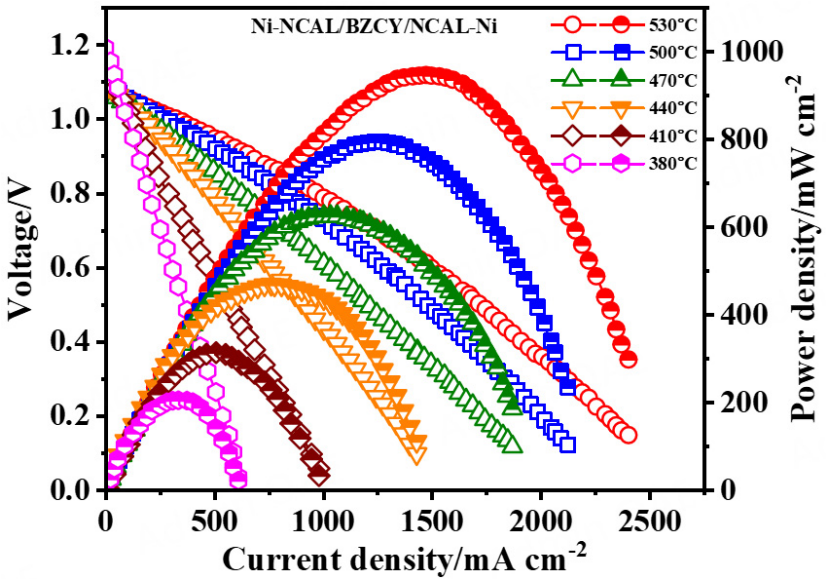

Figure 2. *I-V* and *I-P* curves of the cell devices using BZCY as electrolyte.

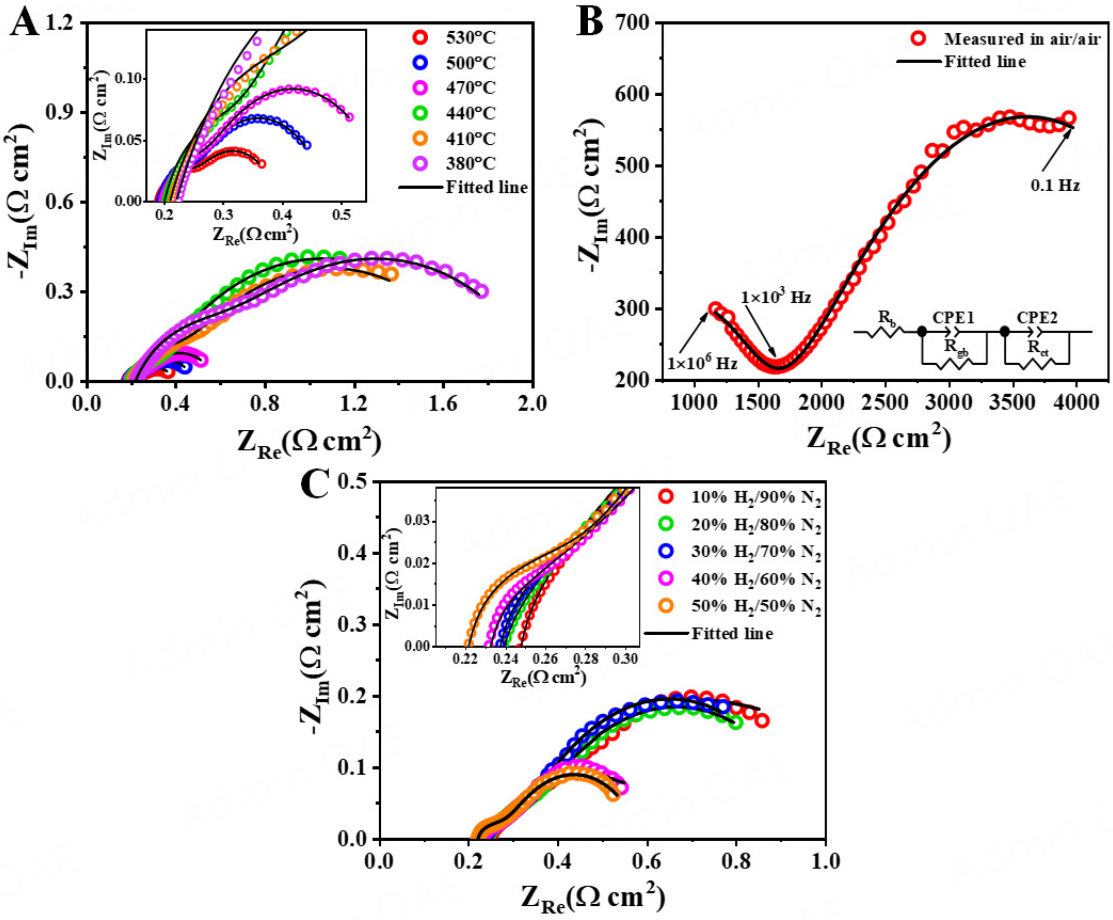

Figure 3. (A) EIS in fuel cell conditions at different temperatures. (B) EIS in air/air atmosphere at 500 °C temperature. (C) EIS in H_2 + N_2 atmosphere with different concentrations of H_2 on both sides at 500 °C temperature.

Similarly, EIS measurements were taken in air/air environment at 500 °C as shown in Figure 3B. The resulting curve gives insight into the cell's behavior in a consistent and controlled oxygen-rich atmosphere, which is useful for understanding the ORR reaction kinetics and the material's overall resistance to oxygen ion transport. Here, calculated R_b, R_{gb} and R_{ct} are 1,020% ± 5%, 757% ± 5% and 2,535% ± 5% Ω cm^2, respectively [Supplementary Table 2]. Since in air/air, ORR is O^{2-} transport as given in following reaction:

$$O_2 + 4e^- \leftrightarrow 2O^{2-} \quad (8)$$

Here, O^{2-} conducting fuel cell ORR is different from H^+ conducting fuel cell ORR. Comparing conductivity in air and H_2 contained atmosphere, it is evidenced that the proton conduction was dominant, 4-5 orders higher. In this case, the ORR is transferred to Equation (6), the H^+ PCFC ORR involving the proton bulk and grain boundary transport through membrane.

Further, Figure 3C demonstrates the EIS spectra for the cell operating in an atmosphere containing a mixture of nitrogen and hydrogen gases (H_2 + N_2) at varying concentrations of hydrogen (H_2) at 500 °C temperature. The curves demonstrate how the cell's impedance is affected by the introduction of hydrogen, indicative of the HOR activity. As the concentration of hydrogen increases, it was seen a decrease in the impedance, reflective of enhanced HOR kinetics. This behavior aligns with the calculated proton transference numbers (t_{H^+} = 0.84-0.94) and oxide ion transference number ($t_{O^{2-}} < 1$) at temperature range of 370-530 °C, confirming that proton conduction is the dominant transport mechanism [Supplementary Figure 2]. Detailed calculations are provided in the Supplementary Material.

A comparative analysis of electrode process, ORR, HOR and ionic transport is presented

(i) Overall process in H_2/air *vs.* in air/air:

In the H_2/air environment, the impedance analysis indicated that the R_{ct} for the overall electrode process was much lower, 4-5 orders of magnitude less than that of the ORR process in the air/air atmosphere. Thus, the electrode processes in the H_2/air atmosphere show much better electrochemical kinetics and lower polarization resistances, likely due to the electrochemical processes not only in the HOR but also ORR in the fuel cell as discussed above. R_{gb} in H_2/air was lower than R_b, proving that grain boundary conduction is higher than bulk conduction. Overall, R_{gb} and R_b in H_2/air was four to five orders lower than in air/air environment.

(ii) Overall process in H_2/air *vs.* in 10%H_2/90%N_2:

In the H_2/air environment, the overall electrode process exhibited lower R_b and R_{gb} compared to the HOR process in the 10%H_2/90%N_2 atmosphere [Supplementary Table 3]. The discrepancies in R_b and R_{gb} values between these comparisons reflect the varying reaction kinetics, transport phenomena, and gas compositions in the two different gas environments. The discrepancy in the R_{gb} values can indeed be attributed to the introduction of protons (H^+) and their involvement in the overall electrochemical reactions. In the H_2/air environment, the introduction of protons facilitates the participation of H^+ in the ORR process, as given in Equation (6). However, it is different in H_2 + N_2 case, where $2H^+ + 2e^- \leftrightarrow H_2$ takes place. Therefore, fuel cell H^+ transported ORR involvement leads to a more efficient and lower R_{ct} and significantly lower R_b and R_{gb}.

Conversely, in the case of the ORR process in the air/air atmosphere, where only the reduction of O_2 to O^{2-} occurs (Equation 8), the absence of the proton's participation resulted in a much higher R_{gb} value, as the reaction occurs without the facilitation of proton transfer. This distinction highlights the significance of the proton's role in influencing the reaction kinetics and the overall R_{ct} within the system.

These findings, particularly the discrepancy in the R_b and R_{gb} values, provide valuable insights into the both HOR and ORR and its role in the different gas environments. The transfer of protons (H^+) in the electrode processes within the H_2/air atmosphere underscores the significance of the charge transfer and transport mechanism in facilitating protons transport and interplay of bulk and grain boundary conduction during the electrochemical reactions.

In the H_2/air environment, the lower R_b and R_{gb} values suggest that the electrochemical process is efficiently promoting the protons transport, contributing to enhanced reaction kinetics and overall lower resistance for HOR and ORR. Therefore, the observed variations in the R_{ct} between these environments are directly related to the efficiency of the reaction kinetics, highlighting its crucial role in governing the overall reaction kinetics and the transport phenomena within the fuel cell system. Understanding the intricacies of the R_{ct} in different gas environments is essential for optimizing the performance and efficiency of fuel cell technologies.

Figure 4A shows the EIS for the assembled cell (Ni-NCAL/BZCY/NCAL-Ni) with 500 °C annealed BZCY electrolyte and 1,500 °C sintered BZCY electrolyte in air atmosphere [Supplementary Tables 4 and 5, respectively]. The bulk and grain boundary resistance of annealed BZCY was much higher than sintered BZCY in air atmosphere. The lower resistance of sintered BZCY may have contributed to a bulk transport mechanism[28]. Annealed BZCY was not sintered to dense ceramic, and it possesses much more particle contacts; thus, grain boundaries hinder the O^{2-} transport in air atmosphere. Opposite trend was observed in Figure 4B, where both bulk and grain boundary resistances of annealed BZCY are significantly lower than those of sintered BZCY in H_2/air atmosphere [Supplementary Tables 6 and 7, respectively]. Notably, in the fuel cell environment (H_2/air), the annealed BZCY exhibited an exceptionally high total conductivity of 0.158 S cm^{-1} at 500 °C [Figure 4C], which is approximately two orders of magnitude higher than that of the sintered BZCY [Figure 4D]. The difference in conductivities between annealed BZCY and sintered BZCY can be attributed to the proton conduction through surface and grain boundary of BZCY particles [Figure 4E and F].

Distribution of relaxation times

Distribution of relaxation times (DRT) analysis was performed at different time scales in air/air and H_2/air environments at a fixed temperature of 500 °C[22,29,30]. This analysis is useful for identification of polarization processes with high resolution and differentiates the electrochemical process that intersects in EIS curves[31]. Figure 5A demonstrates the DRT results of NCAL|BZCY|NCAL cell from air/air to H_2/air atmosphere and proton injection took place from 5 to 50 min where conductivities become relatively stable. A low flow rate of H_2 and air at 20 mL min^{-1} was used. Different peaks indicate different electrochemical processes. Peaks have been fitted to calculate the peak areas by integration that is related to the polarization resistance of a single process[32]. Area and frequencies of each peak in air/air were calculated and presented in Supplementary Table 8. Meanwhile, peak area and frequencies in H_2/air were calculated and presented in Supplementary Tables 9 and 10, respectively. This analysis will allow us to deconvolute and understand the complex electrochemical reactions and transport processes within the fuel cell, and their dependency on the operating environment and time. It is also pivotal for optimizing fuel cell design and operation to improve efficiency and performance.

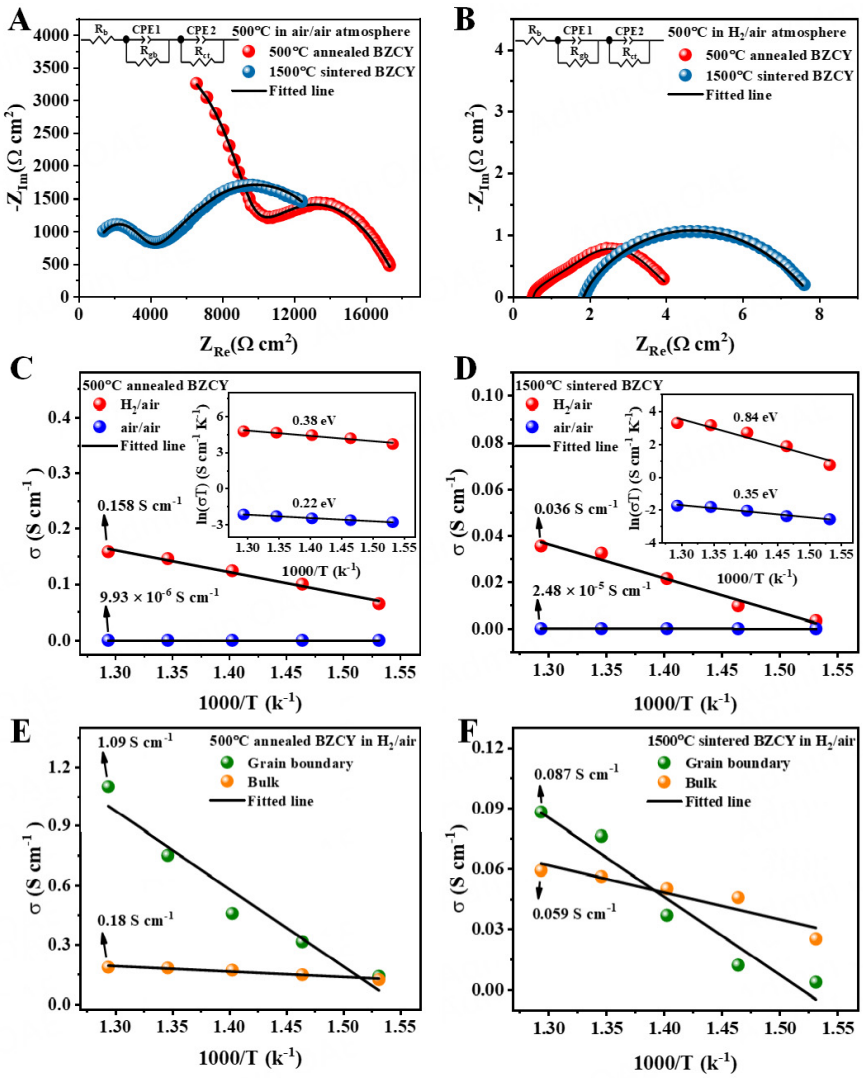

Figure 4. EIS spectra of cell with 500 °C annealed BZCY electrolyte, 1,500 °C sintered BZCY electrolyte. (A) in air/air atmosphere at 500 °C, (B) in a H_2/air atmosphere at 500 °C, (C) Total (bulk + grain boundary) conductivity and Arrhenius plots of cells with 500 °C annealed BZCY in H_2/air and air atmospheres, (D) Total conductivity and Arrhenius plots of cells with 1,500 °C sintered BZCY in H_2/air and air atmospheres, (E) bulk and grain boundary conductivity of cell with 500 °C annealed BZCY in H_2/air atmospheres, (F) Bulk and grain boundary conductivity of cell with 1,500 °C sintered BZCY in H_2/air atmospheres.

In the air/air environment, six peaks are shown: P1′, P2′, P3′, P4′, P5′ and P6′ at different time scales [Figure 5A]. Here, P1′ represents the charge transfer in the electrodes, P2′ denotes the transfer of oxide ions at the electrode/electrolyte interface, P3′ corresponds to oxygen incorporation to lattice, while P4′ is related to oxygen reduction to oxygen ion (ORR) as given in Equation (8), P5′ corresponds to oxygen adsorption and dissociation and P6′ shows gas diffusion[31,33]. After proton injection, seven peaks are observed but at different time scales as we can see from Figure 5A. By analyzing frequencies from Supplementary Table 10, P1 represents the proton interfacial conduction and incorporation to lattice, P2 corresponds hydrogen dissociation and proton formation (HOR)[34,35]. Peaks P3 appear at intermediate frequencies, demonstrating the oxygen incorporation into lattice and bulk diffusion of protons into the triple phase boundary (TPB)[31,33]. P4 corresponds to ORR process by air side as expressed by Equation (6). Based on the location and time scales analysis for peaks in air/air and H_2/air, P5 and P6 are related to oxygen adsorption and dissociation, and last peak P7 corresponds to polarization due to gas diffusion[31,33].

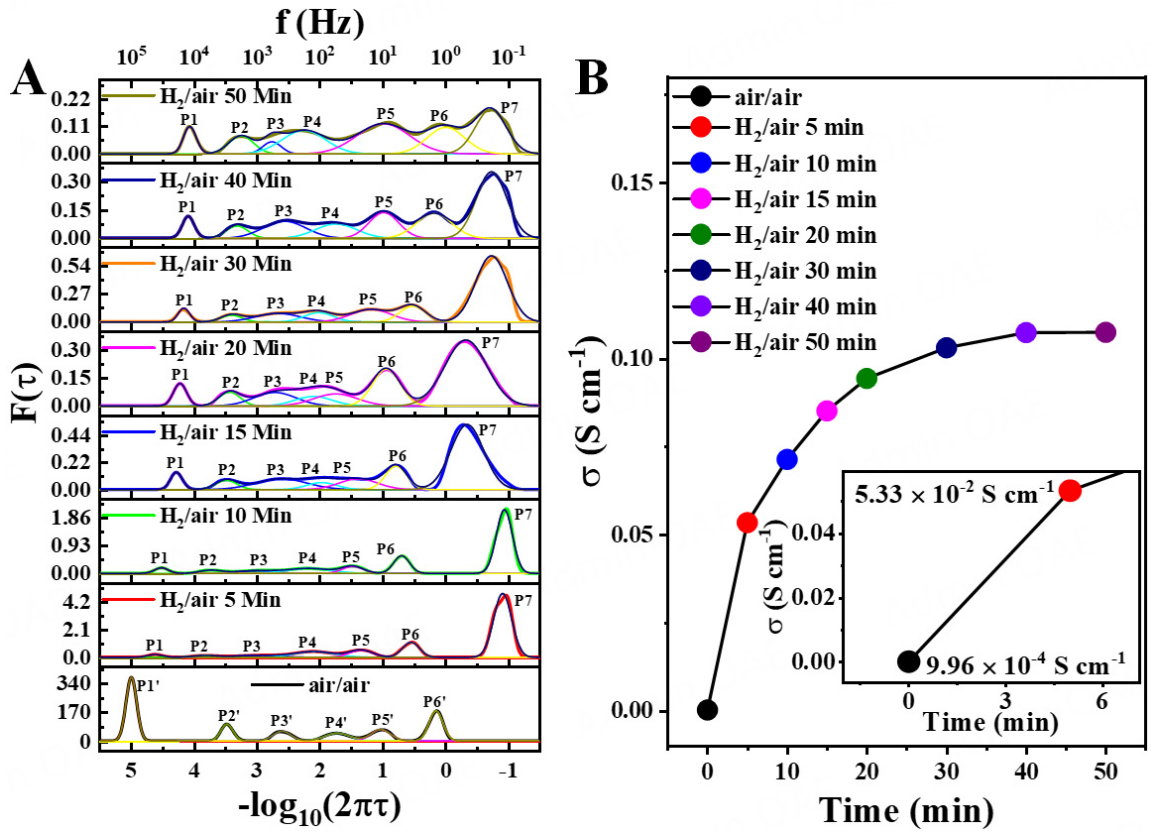

Figure 5. (A) DRT results of air/air and H_2/air from 5 to 50 min at 500 °C. (B) conductivities calculated from air/air to H_2/air environment for 50 min.

When one side of air was replaced with H_2, areas under all peaks decrease significantly. Peak P1′ shifted to P1 and area under curve started decreasing from 79.965 to 0.054509 Ω cm^2 in first 5 min and stabilizes at 0.02795 Ω cm^2 in 50 min and frequency also stabilizes, which indicates that polarization is four orders easier to proceed. It further shows that HOR ($H_2 \leftrightarrow 2H^+ + 2e^-$) occurred at anode and protons are injected into BZCY reaching at cathode to participate in the ORR. More specifically, comparing the areas of peaks P4′ and P4, it was observed that corresponding polarization under air is 21.286 Ω cm^2 which rapidly decreases to 0.3542 Ω cm^2 within 5 min after proton injection during fuel cell process. Also, frequency abruptly increases from 53.79057 to 129.3178 Hz. Accreted ORR after proton injection demonstrates that ORR process accelerated with proton injection[36]. It further showed that polarization losses were minimized with injection of protons, which lowers the energy barriers and driving forces for electrochemical reactions. This results in faster electrocatalytic activity and more efficient electrode reactions. From Figure 5A, it was noticed that frequency of peak P1′ in air/air is 100,378.8 Hz which is very high, but when protons are injected the peak shifts to P1 and frequency drops to 41,753.18 Hz which further stabilizes at 12,080.97 Hz in next 50 min. P2 and P4 showing the electrochemical process involved in HOR and ORR can create a more complex dynamic that affects the relaxation behavior.

Figure 5B depicts the change in conductivity of a fuel cell when the atmosphere is switched from air/air to H_2/air and measured over a period of 50 min after proton injection. Conductivities were calculated from EIS data. Total conductivity in air was 9.96×10^{-4} S cm^{-1} before supplying H_2. Upon switching one side to a hydrogen atmosphere, there was a marked increase in conductivity, illustrated by the upward trend in the data points. In the first 5 min of proton injection, conductivity increases quickly from 9.96×10^{-4} to

5.3×10^{-2} S cm^{-1} and then rate of change gradually slows down until the conductivity stabilizes at 0.109 S cm^{-1} in 50 min of proton injection. Notably, with the introduction of hydrogen, migration of protons in the electrolyte increases, further increasing cell conductivity[37]. Further conductivity changes greatly from air/air to H_2/air (FC) environment, which hints that an EPI process takes place because of the absence of initial proton concentration in the air/air environment.

Impedance plots are very complex to resolve for each process using equivalent circuit models. Therefore, a combined approach viz., analysis of EIS curves using equivalent circuit model along with DRT results (EIS-DRT) has been used to resolve the complexity of the impedance data. Equation (7) is used to calculate the characteristic capacitance and time constants are calculated using

$$RC = \tau \tag{9}$$

Figure 6 shows complex plane impedance diagrams and corresponding DRT plots from air/air to H_2/air environment after 5 and 50 min of proton injection. The obtained impedance plots comprised of grain boundary and electrode process arcs. The peak P1′ in Figure 6A, corresponds to the C_1 (2.49×10^{-7} F cm^{-2}) which is ascribed to grain boundary arc and its relaxation time is 9.96×10^{-6} s. The remaining portion of the impedance spectra with C values (10^{-6}-10^{-3} F cm^{-2}) and relaxation times (10^{-4}-0.72 s) corresponds to various electrode processes[34,37]. Comparison of Figure 6A-C shows that capacitance C_1 of P1 increases to 8.97×10^{-4} F cm^{-2} after 50 min of proton injection with time constant of 4.1×10^{-5} s and corresponding resistance also decreases. Starting points and area under peaks P1 of both Figure 6B and C decrease with time which clearly elaborates that bulk and grain boundary resistances decrease. It is observed that time constant τ increase to some extent possibly due to the both bulk and grain boundary conduction. The higher capacitance observed under H_2/air can be attributed to introducing external protons into BZCY mainly in grain boundaries, which cause a dual consequences of charge storage and dipolar polarization, thus higher capacity. Conversely, under air/air conditions, absence of protons results in a significantly reduced capacitance. Corresponding time constants and capacitances for air/air, 5 and 50 mins of proton injection are shown in Supplementary Table 11.

Randles circuit is a widely used equivalent circuit for analyzing electrochemical systems. To include the electronic contributions in a mixed ionic and electronic conductors (MIEC) system, an additional element can be added in parallel with the ionic resistance (R_i) element. This parallel element represents the electronic resistance (R_e) associated with the electronic conduction in the MIEC materials[38,39]. This circuit model consists of two-time constants and is often used to represent systems with both electronic and ionic processes. One time constant (τ_1) represents ionic processes, such as diffusion in the electrolyte materials and the other time constant (τ_2) represents the electronic processes, such as charge transfer at the electrode-electrolyte interface. In addition, Z_w is commonly used to describe diffusion-limited processes in EIS. It appears as a diagonal line with a slope of 45° on a Nyquist plot. In MIEC systems, the Z_w can represent both ionic and electronic diffusion processes. The two-time constants obtained from EIS by using Equation (9) and fitted results are shown in Supplementary Table 12.

In Figure 7A, the red curve indicates the impedance response of the fuel cell in a stable, oxygen-rich environment. This configuration shows a combination of high-frequency resistance which is related to the electrolyte and other components' ohmic resistance, a medium-frequency semicircle corresponding to R_{ct} at the electrodes, and a low-frequency Warburg tail indicative of diffusion processes. While in Figure 7B, the green curve represents the EIS response shortly after introducing hydrogen into the system (5 min) and blue curve after extended period of operation (50 mins). Upon the introduction of hydrogen, changes in the size

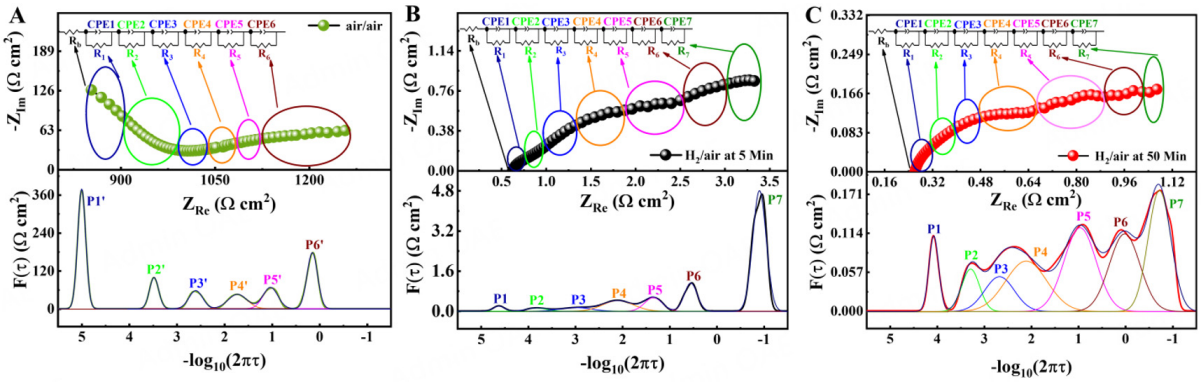

Figure 6. Complex-plane impedance diagrams and corresponding distribution of relaxation time plots (EIS-DRT) at 500 °C with $R_b \perp (R_1 \| C_1) \perp (R_2 \| C_2) \perp (R_3 \| C_3) \perp (R_4 \| C_4) \perp (R_5 \| C_5) \perp (R_6 \| C_6)$ circuit model in (A) air/air, (B) With $R_b \perp (R_1 \| C_1) \perp (R_2 \| C_2) \perp (R_3 \| C_3) \perp (R_4 \| C_4) \perp (R_5 \| C_5) \perp (R_6 \| C_6) \perp (R_7 \| C_7)$ 5 min after supplying H_2/air, and (C) 50 min after supplying H_2/air.

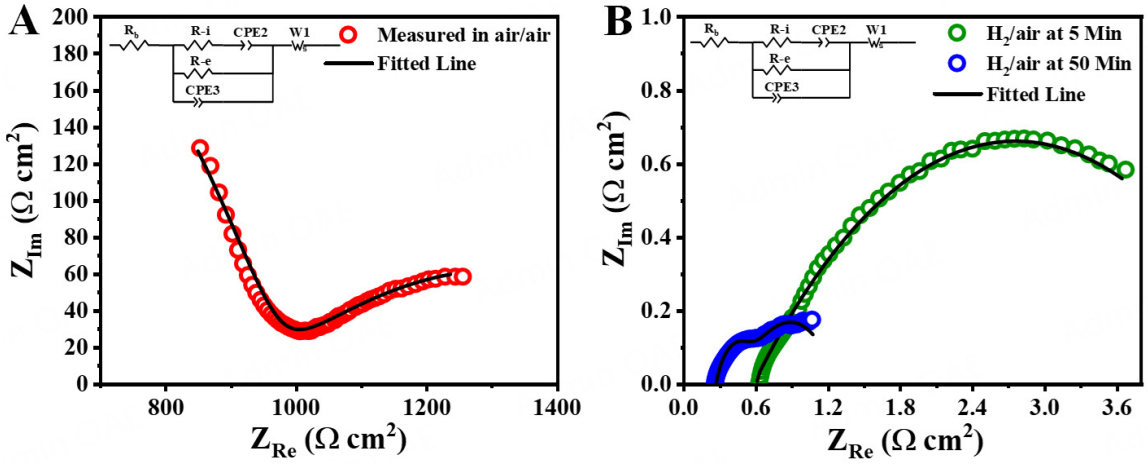

Figure 7. Fitted EIS using modified Randles Circuit element in (A) air/air, (B) at 5 Min and 50 Min of H_2/air.

and position of the semicircle in the EIS plot were observed, reflecting the different electrochemical dynamics.

From air/air to H_2/air, R_i decreases from 231.2 to 0.124 which is a clear sign that proton injection decreases the R_i and R_e also decreases from 410.4 to 0.70, respectively. We can say that proton injection simultaneously promotes both ionic and electronic processes. Further by comparing the time constants of EIS results with DRT analysis in Figure 5A, it was observed that τ_1 is related to Peak P1, which further shows that P1 belongs to ionic diffusion in the electrolyte. In air/air, τ_2 is 1.2×10^{-2} which increases to 0.18 after 50 mins of proton injection. From DRT results, P5′ and P6 shows almost same time constant which shows the oxygen dissociation.

Warburg resistance is very high in air/air and its value is 320; it also decreases in H_2/air environment and its value is 0.221 after 50 mins. In addition, W-T in air is 0.0698 and decreases to 0.00364 after proton injection. Lower values of W-R and W-T in H_2/air clearly show that proton injection facilitates the diffusion process. This analysis can help to understand the kinetics of the reactions at the electrodes (HOR at the anode and ORR at the cathode), to guide the optimization of fuel cell materials and operation conditions for improved performance.

Further, experiments are performed to calculate the activation energies in different atmospheres. Figure 8A shows the conductivity and Arrhenius plot of the cell in different environments, while Figure 8B explains the alteration in energy landscape and reaction progress in different environments. Activation energy for ORR reaction in air/air is 0.88 eV which is quite high, and it decreases to 0.45 eV for HOR in the oxidizing environment (H_2 + N_2). There is a significant transition in the H_2/air and the activation energy for proton transport was determined to be 0.29 eV[40]. Additionally, the proton conductivity was measured to be 0.19 S cm^{-1} at 530 °C, indicating efficient proton transport through bulk and grain boundaries[37]. It demonstrates that in H_2/air environment, interplay of bulk and grain boundary proton transport promotes reaction progress, leading to lower the activation energy. The observed alterations in energy landscape highlight crucial role of HOR, ORR and proton transport in governing overall reaction kinetics. Understanding of energy landscape in different gas environments is essential for optimizing fuel cell performance and efficiency.

The utilization of BZCY has been shown to lower the activation energies required for both HOR and ORR, facilitating a more effective energy conversion process and rendering the PCFC system more viable for widespread adoption. This achievement is notably pronounced at reduced temperatures, addressing a significant challenge in the field of fuel cell technology and opening avenues for energy-efficient, eco-friendly power sources. As a result, the fuel cell device under investigation, along with its specific measurement conditions, deviates notably from traditional fuel cell studies. We obtain valuable insights into the electrochemical process of proton injection, elucidating the occurrences of grain boundary proton conduction phenomena. More specifically, this analysis discloses that ORR process is shifted from O^{2-} ($O_2 + 4e^- \leftrightarrow 2O^{2-}$) to proton dominated $2H^+ + 1/2O_2 + 2e^- \leftrightarrow H_2O$.

The research conducted on PCFCs utilizing BZCY electrolytes has revealed a myriad of electrochemical phenomena critical to the enhancement of fuel cell performance. Our study has delved into the core electrochemical processes of the HOR and ORR, uncovering the substantial impact that these reactions, governed by BZCY's unique properties, have on the cell's efficacy, particularly at low operating temperatures (300-500 °C). The electrochemical analysis has been indispensable in understanding the intrinsic kinetics and dynamics that govern these reactions. The insights gained point towards the possibility of tailoring electrolyte and electrode materials to further harness the potential of proton conduction, thereby optimizing the operational parameters of PCFCs. Future studies will likely continue to build upon the foundation established by this work, exploring the vast landscape of material science and electrochemistry to refine the capabilities of PCFCs. The progress in this field has the potential to make a meaningful contribution to the energy sector, propelling us towards a future where sustainable energy solutions are not just envisioned but fully realized. This investigation underscores the indispensable role of comprehensive electrochemical analyses in enhancing the performance of proton-conducting fuel cells. With BZCY as a cornerstone material, we step closer to the actualization of highly efficient and environmentally benign energy systems suitable for a range of applications, from portable power to large-scale energy distribution.

CONCLUSION

We have introduced a new electrochemical method, EPI, to successfully improve material properties and delve into the interplay between electrochemical performance and material characteristics. Our results reveal that the optimized BZCY electrolyte, coupled with device-level innovations, can achieve significantly better performance metrics than conventional BZCY-based PCFCs. The findings also highlight the ability of BZCY to significantly lower the activation energies for key reactions, including the HOR and ORR. This

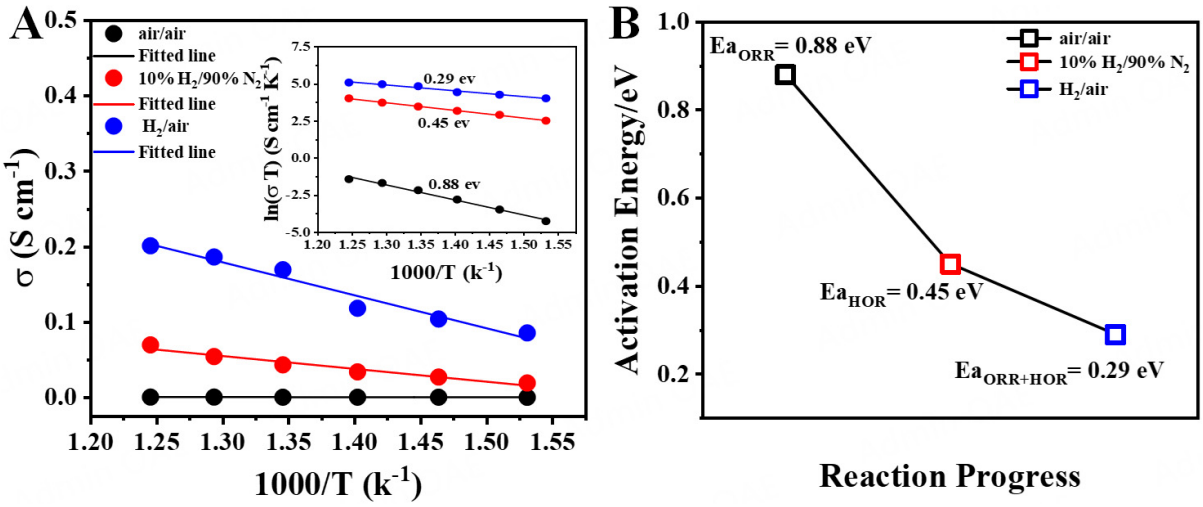

Figure 8. (A) Conductivity and Arrhenius plot in air/air, 10% H_2 / 90% N_2 and H_2/air environments, (B) alteration in energy landscape and reaction progress in gas different environments.

advancement not only enhances energy conversion efficiency but also demonstrates BZCY's potential in advancing the practical application of PCFCs. Moreover, this study underscores the necessity of intricate electrochemical analysis and approaches to improve material properties and pinpoint the dynamic interplay of reactions within PCFCs. Future research, building on these insights, will further explore material modifications to enhance proton conductivity and overall cell performance. The progress made in this study brings us closer to achieving sustainable and eco-friendly energy solutions, which are pivotal for our evolving energy landscape.

DECLARATIONS

Authors contributions

Conceptualization, investigation: Anwar, M. F.; Yu, Y.; Asghar, M. I.; Zhu, B.
Methodology: Anwar, M. F.; Yu, Y.; Zhu, B.
Writing - original draft: Anwar, M. F.; Zhu, B.
Writing review & editing: Zhu, B.; Asghar, M. I.; Huang, J.; Khalid, M.; Bibi, B.; Nazar, A.; Sarfraz, M. F.
Funding acquisition, resources, supervision: Zhu, B.

Availability of data and materials

The data that support the findings of this study are available from the corresponding author upon reasonable request.

Financial support and sponsorship

This work was supported by the Basic Science Center Program for Ordered Energy Conversion (No. 52488201), the key project (No. 52336009) of NSFC Science and Technology Department of Jiangsu Province (Grant BE2022029), Research Council of Finland (Grant No. 13329016, 13322738, 13352669).

Conflicts of interest

The editorial decision for this manuscript follows a double-blind review process. Zhu, B., the Co-Editor-in-Chief of *Energy Materials*, is not involved in any stage of the editorial process, including reviewer selection, manuscript handling, or decision-making, while all other authors have declared no conflicts of interest.

Ethical approval and consent to participate

Not applicable.

Consent for publication

Not applicable.

Copyright

REFERENCES

1. Nasani, N.; Ramasamy, D.; Antunes, I.; Perez, J.; Fagg, D. P. Electrochemical behaviour of Ni-BZO and Ni-BZY cermet anodes for protonic ceramic fuel cells (PCFCs) - A comparative study. *Electrochim. Acta.* **2015**, *154*, 387-96. DOI
2. Duan, C.; Kee, R. J.; Zhu, H.; et al. Highly durable, coking and sulfur tolerant, fuel-flexible protonic ceramic fuel cells. *Nature* **2018**, *557*, 217-22. DOI
3. Choi, S.; Kucharczyk, C. J.; Liang, Y.; et al. Exceptional power density and stability at intermediate temperatures in protonic ceramic fuel cells. *Nat. Energy.* **2018**, *3*, 202-10. DOI
4. Iwahara, H.; Esaka, T.; Uchida, H.; Maeda, N. Proton conduction in sintered oxides and its application to steam electrolysis for hydrogen production. *Solid. State. Ion.* **1981**, *3-4*, 359-63. DOI
5. Iwahara, H.; Uchida, H.; Ono, K.; Ogaki, K. Proton conduction in sintered oxides based on $BaCeO_3$. *J. Electrochem. Soc.* **1988**, *135*, 529-33. DOI
6. Murakami, T.; Hester, J. R.; Yashima, M. High proton conductivity in $Ba_5Er_2Al_2ZrO_{13}$, a hexagonal perovskite-related oxide with intrinsically oxygen-deficient layers. *J. Am. Chem. Soc.* **2020**, *142*, 11653-7. DOI PubMed
7. Wei, T.; Zhang, L. A.; Chen, Y.; Yang, P.; Liu, M. Promising proton conductor for intermediate-temperature fuel cells: $Li_{13.9}Sr_{0.1}Zn(GeO_4)_4$. *Chem. Mater.* **2017**, *29*, 1490-5. DOI
8. Garcia-Barriocanal, J.; Rivera-Calzada, A.; Varela, M.; et al. Colossal ionic conductivity at interfaces of epitaxial ZrO_2: Y_2O_3/$SrTiO_3$ heterostructures. *Science* **2008**, *321*, 676-80. DOI
9. Xing, Y.; Wu, Y.; Li, L.; et al. Proton shuttles in CeO_2/$CeO_{2-\delta}$ core-shell structure. *ACS. Energy. Lett.* **2019**, *4*, 2601-7. DOI
10. Chen, G.; Sun, W.; Luo, Y.; et al. Advanced fuel cell based on new nanocrystalline structure $Gd_{0.1}Ce_{0.9}O_2$ electrolyte. *ACS. Appl. Mater. Interfaces.* **2019**, *11*, 10642-50. DOI
11. Liu, X.; Dong, W.; Tong, Y.; et al. Li effects on layer-structured oxide $Li_xNi_{0.8}Co_{0.15}Al_{0.05}O_{2-\delta}$: improving cell performance via on-line reaction. *Electrochim. Acta.* **2019**, *295*, 325-32. DOI
12. Duan, C.; Kee, R.; Zhu, H.; et al. Highly efficient reversible protonic ceramic electrochemical cells for power generation and fuel production. *Nat. Energy.* **2019**, *4*, 230-40. DOI
13. Pei, K.; Zhou, Y.; Xu, K.; et al. Surface restructuring of a perovskite-type air electrode for reversible protonic ceramic electrochemical cells. *Nat. Commun.* **2022**, *13*, 2207. DOI PubMed PMC
14. Ni, M.; Shao, Z. Fuel cells that operate at 300° to 500 °C. *Science* **2020**, *369*, 138-9. DOI PubMed
15. Zhou, X.; Yang, J.; Wang, R.; Zhang, W.; Yun, S.; Wang, B. Advances in lithium-ion battery materials for ceramic fuel cells. *Energy. Mater.* **2022**, *2*, 200041. DOI
16. Chen, G.; Sun, W.; Luo, Y.; et al. Investigation of layered $Ni_{0.8}Co_{0.15}Al_{0.05}LiO_2$ in electrode for low-temperature solid oxide fuel cells. *Int. J. Hydrogen. Energy.* **2018**, *43*, 417-25. DOI
17. Yuan, K.; Yu, Y.; Lu, X.; Ji, X.; Zhu, B. A new technology for spraying advanced low-temperature (300 ~ 600 °C) solid oxide fuel cells. 2017, pp. 132-7. DOI
18. He, Y.; Chen, G.; Zhang, X.; et al. Mechanism for major improvement in SOFC electrolyte conductivity when using lithium compounds as anode. *ACS. Appl. Energy. Mater.* **2020**, *3*, 4134-8. DOI
19. Xia, C.; Afzal, M.; Wang, B.; et al. Mixed-conductive membrane composed of natural hematite and $Ni_{0.8}Co_{0.15}Al_{0.05}LiO_{2-\delta}$ for electrolyte layer-free fuel cell. *Adv. Mater. Lett.* **2017**, *8*, 114-21. DOI
20. Park, H. C.; Virkar, A. V. Bimetallic (Ni-Fe) anode-supported solid oxide fuel cells with gadolinia-doped ceria electrolyte. *J. Power. Sources.* **2009**, *186*, 133-7. DOI
21. Yu, Y.; Shah, M. Y.; Wang, H.; et al. Synergistic proton and oxygen ion transport in fluorite oxide-ion conductor. *Energy. Mater. Adv.* **2024**, *5*, 0081. DOI
22. Zhang, Y.; Chen, Y.; Yan, M.; Chen, F. Reconstruction of relaxation time distribution from linear electrochemical impedance spectroscopy. *J. Power. Sources.* **2015**, *283*, 464-77. DOI
23. Wang, J.; Huang, Q. A.; Li, W.; et al. Insight into the origin of pseudo peaks decoded by the distribution of relaxation times/ differential capacity method for electrochemical impedance spectroscopy. *J. Electroanal. Chem.* **2022**, *910*, 116176. DOI
24. Wang, J.; Huang, Q. A.; Wang, J.; Zhang, J. Shape factor optimisation for the distribution of relaxation times to better deconvolute electrochemical impedance spectra. *J. Electroanal. Chem.* **2024**, *962*, 118272. DOI
25. Norbya, T. Proton conduction in oxides. *Solid. State. Ion.* **1990**, *40-1*, 857-62. DOI

26. Uchida, H.; Tanaka, S.; Iwahara, H. Polarization at Pt electrodes of a fuel cell with a high temperature-type proton conductive solid electrolyte. *J. Appl. Electrochem.* **1985**, *15*, 93-7. DOI
27. He, F.; Wu, T.; Peng, R.; Xia, C. Cathode reaction models and performance analysis of $Sm_{0.5}Sr_{0.5}CoO_{3-\delta}$-$BaCe_{0.8}Sm_{0.2}O_{3-\delta}$ composite cathode for solid oxide fuel cells with proton conducting electrolyte. *J. Power. Sources.* **2009**, *194*, 263-8. DOI
28. Duan, C.; Huang, J.; Sullivan, N.; O'Hayre, R. Proton-conducting oxides for energy conversion and storage. *Appl. Phys. Rev.* **2020**, *7*, 011314. DOI
29. Hayd, J.; Ivers-Tiffée, E. Detailed electrochemical study on nanoscaled $La_{0.6}Sr_{0.4}CoO_{3-\delta}$ SOFC thin-film cathodes in dry, humid and CO_2-containing atmospheres. *J. Electrochem. Soc.* **2013**, *160*, F1197-206. DOI
30. Zhang, Y.; Chen, Y.; Li, M.; Yan, M.; Ni, M.; Xia, C. A high-precision approach to reconstruct distribution of relaxation times from electrochemical impedance spectroscopy. *J. Power. Sources.* **2016**, *308*, 1-6. DOI
31. Wang, X.; Ma, Z.; Zhang, T.; et al. Charge-transfer modeling and polarization DRT analysis of proton ceramics fuel cells based on mixed conductive electrolyte with the modified anode-electrolyte interface. *ACS. Appl. Mater. Interfaces.* **2018**, *10*, 35047-59. DOI
32. Li, M.; Sun, Z.; Yang, W.; et al. Mechanism for the enhanced oxygen reduction reaction of $La_{0.6}Sr_{0.4}Co_{0.2}Fe_{0.8}O_{3-\delta}$ by strontium carbonate. *Phys. Chem. Chem. Phys.* **2016**, *19*, 503-9. DOI
33. Wang, J.; Li, Z.; Zang, H.; et al. $BaZr_{0.1}Fe_{0.9-x}Ni_xO_{3-\delta}$ cubic perovskite oxides for protonic ceramic fuel cell cathodes. *Int. J. Hydrogen. Energy.* **2022**, *47*, 9395-407. DOI
34. Yu, S.; Wang, Z.; Yang, L.; et al. Enhancing the sinterability and electrical properties of $BaZr_{0.1}Ce_{0.7}Y_{0.2}O_{3-\delta}$ proton-conducting ceramic electrolyte. *J. Am. Ceram. Soc.* **2021**, *104*, 329-42. DOI
35. Guo, R.; Li, D.; Guan, R.; et al. Sn-Dy-Cu triply doped $BaZr_{0.1}Ce_{0.7}Y_{0.2}O_{3-\delta}$: a chemically stable and highly proton-conductive electrolyte for low-temperature solid oxide fuel cells. *ACS. Sustain. Chem. Eng.* **2022**, *10*, 5352-62. DOI
36. Zhu, B.; Mi, Y.; Xia, C.; et al. A nanoscale perspective on solid oxide and semiconductor membrane fuel cells: materials and technology. *Energy. Mater.* **2022**, *1*, 100002. DOI
37. Wan, S.; Shah, M. A. K. Y.; Wang, H.; Lund, P. D.; Zhu, B. Exceptionally high proton conductivity in Eu_2O_3 by proton-coupled electron transfer mechanism. *iScience* **2024**, *27*, 108612. DOI PubMed PMC
38. Wang, S.; Yan, M.; Li, Y.; Vinado, C.; Yang, J. Separating electronic and ionic conductivity in mix-conducting layered lithium transition-metal oxides. *J. Power. Sources.* **2018**, *393*, 75-82. DOI
39. Moździerz, M.; Dąbrowa, J.; Stępień, A.; et al. Mixed ionic-electronic transport in the high-entropy $(Co,Cu,Mg,Ni,Zn)_{1-x}Li_xO$ oxides. *Acta. Mater.* **2021**, *208*, 116735. DOI
40. Qiao, Z.; Xia, C.; Cai, Y.; et al. Electrochemical and electrical properties of doped CeO_2-ZnO composite for low-temperature solid oxide fuel cell applications. *J. Power. Sources.* **2018**, *392*, 33-40. DOI